Check for updates

High-response humidity sensing with graphene oxide/lignosulfonate and laser-induced graphene for respiratory health†

Yanbo Peng, Yuhong Zhao, Ying Yuan, Wei Meng, Wenhe Jiang and Xiluan Wang [ID] *

Most current commercial humidity sensors rely on precious metals and chemicals. In this study, alkali lignin produced in the paper industry was utilized to form a film with hydroxyethyl cellulose to generate laser-induced graphene (LIG) as an electrode material for a sensor by the laser-induction technique. LIG exhibits excellent conductivity, and the experimental results demonstrate that its resistivity can be adjusted by laser power without the necessity for additional conductive materials. A solution comprising a blend of graphene oxide and sodium lignosulfonate was introduced to the LIG surface in a dropwise manner, thereby establishing a sensing surface. This process resulted in the introduction of hydrophilic groups, including carboxyl, phenolic hydroxyl, and sulfonic acid. The integration of these hydrophilic groups enhanced the surface's sensitivity to humidity, thereby facilitating the precise capture of alterations in ambient air humidity. The humidity sensor, which employs alkali lignin and lignin laser-induced graphene as electrodes and graphene oxide (GO) as the humidity-sensitive layer, exhibits an exceptionally high degree of sensitivity to humidity. The response reached 42.74 (R_{RH}/R_0) at 80% relative humidity and 133.96 (R_{RH}/R_0) at 90% humidity with a sensitivity of 147.73%/% RH. Moreover, the sensor displays an impressively brief recovery period, which remains unaltered even after multiple cycles. Additionally, the humidity sensor exhibits excellent stability for a period of up to 30 days. This study has successfully developed a simple and efficient method for preparing graphene, and has produced a flexible resistive sensor with high sensitivity, repeatability, and stability, thereby opening up new avenues for the high-value utilisation of lignin.

Introduction

Humidity sensors are of great importance in the field of agriculture,[1] industrial production and human activities.[2,3] Researchers have investigated a multitude of humidity detection mechanisms, including resistors, photoreactors, capacitors, field effect transistors (FETs), and quartz crystal microbalances (QCMs).[4–7] Among the existing sensing technologies, resistive sensors are worthy of further investigation due to their straightforward structure, cost-effectiveness and straightforward circuit design. To enhance the sensing performance, a plethora of novel sensing materials have been developed, encompassing carbon materials,[8,9] electrospun fibres,[10] metal oxides,[11,12] semiconductor particles[13] and composite nanomaterials.[14] Nevertheless, the primary impediments to the industrialisation of sensors are the elevated cost of electrodes, the high cost of raw materials and the intricate nature of the manufacturing process. The large-scale development of low-

cost humidity sensing materials represents a significant challenge.

Lignin has low intrinsic value and a low utilization rate.[15] But most of lignin is burned as fuel, and only a small part of lignin is converted into commercial products.[16] However, about 50 million tons of lignin are produced worldwide through industrial and biological refining processes every year.[17] As the second largest natural polymer on the earth, lignin is the most important source of aromatic biomass. Its antioxidant, antibacterial, biodegradable, and CO_2-neutral properties have garnered increasing attention. With the emergence of environmental pollution and resource crisis, the effective utilization of lignin has attracted increasing attention, because it not only brings economic benefits to the biomass industry, but also helps to reduce the dependence on fossil energy.[18,19] Through previous studies, modern lignin extraction technology has been developed and mature, mainly used to prepare high value-added products such as pyrolysis oil,[20] phenolic resin, polyurethane, epoxy resin and heavy metal adsorbent.[16,21,22] The current research project is focused on the preparation of graphene from woody biomass resources, including wood and paper, using laser etching.[23] Nevertheless, the considerable heterogeneity of lignin represents a significant obstacle to the

Beijing Key Laboratory of Lignocellulosic Chemistry, Beijing Forestry University, Beijing, 100083, P. R. China. E-mail: wangxiluan@bjfu.edu.cn

† Electronic supplementary information (ESI) available. See DOI: https://doi.org/10.1039/d5ra01765c

large-scale utilisation of lignin-based materials, particularly those based on graphene. Fortunately, laser etching technology can effectively circumvent the influence of lignin heterogeneity, thereby enabling the efficient preparation of graphene.[24]

The disposal and recycling of electronic products also present long-term challenges, as traditional electrodes are often composed of expensive and non-recyclable metals, including copper, gold, silver, platinum, nickel, chromium and aluminium.[25,26] Research in the field of humidity sensors has seldom addressed the electrode component. Lignin-derived laser-induced graphene (LIG) represents an optimal electrode material, offering a cost-effective and renewable alternative. Furthermore, industrial lignin can be transformed into water-soluble lignosulfonate (LS), which is rich in hydrophilic groups, through sulfonation.[27] This material has attracted considerable interest due to its renewability, low cost and potential as a surfactant and water adsorbent. The functionality of resistive humidity sensors depends on changes in ambient humidity signal.[28] Chemical resistance materials, as potential materials for wearable sensors, can directly convert external stimuli into electrical signals for detection. It boasts a straightforward structure, simple signal collection, and straightforward manufacturing.[10,29,30] Moreover, the sensitivity of such sensors can be markedly enhanced by the introduction of hydrophilic groups, including carboxyl groups, phenolic hydroxyl groups, and sulfonic acid groups. Graphene is a low-dimensional material with superior electrical sensitivity and a large surface-to-volume ratio, which renders it a promising candidate for incorporation into low-dimensional humidity sensing materials.[31–34] Graphene oxide (GO), a derivative of graphene, exhibits excellent hydrophilicity owing to the existence of epoxy, hydroxyl, and carboxyl groups on its surface and edges.[35,36] This property endows GO with a remarkable capacity for humidity sensing. Further improvements to the humidity sensor's performance may be achieved through modifications to the sensitive layer.[37]

Expanding the response range of sensor to humidity and reducing their response and recovery times have always been focal points in sensor research. Alrammouz deposited aluminum IDE onto highly porous GO-coated cellulose paper, created by immersing the paper in a GO solution *via* vacuum thermal evaporation, and subsequently designed a capacitive humidity sensor. While this sensor is capable of reducing resistivity, its sensing humidity range is limited to only 30% to 90%.[38] Zhu developed a humidity sensor utilizing a blend of nanocellulose and carbon nanotubes as the moisture-sensitive material. Although this sensor's response humidity range has been expanded to 11–95%, its response/recovery times are quite lengthy, at 330 s/377 s respectively.[9] Through *in situ* polymerization, hydrophilic PANI with varying concentrations was coated onto the surface of nanofibers, subsequently enabling the assembly of a resistive humidity sensor. The sensor's humidity response range can be enhanced from the original 49% to 83%, with a response/recovery time of 33/88 seconds.[39] Sulfides such as MoS_2 are also widely used in humidity sensors.[40] A flexible humidity sensor was developed on textiles using silver conductive ink and carbon conductive ink through screen printing technology. It has preferably linear response in the humidity range of 28.8–91.5%, but its response recovery time at the highest humidity is 20 s and 35 s respectively.[1]

This study presents the design of a lignin-based laser-induced graphene electrode, which incorporates graphene oxide as a humidity-sensitive layer and integrates LS as a moisture-absorbing enhancement material. The experimental outcomes indicate a response of 41.74 (R_{RH}/R_0) at 80% relative humidity (RH), approximately tripling that of a pristine graphene oxide film. Furthermore, the peak response observed at 90% RH was 132.96 (R_{RH}/R_0), with a sensitivity of 147.73%/% RH.

The field of humidity sensing technologies is experiencing continuous refinement and enhancement, particularly within the domains of industrial Internet of Things and healthcare. Despite the progress made by commercial capacitive polymer and MEMS sensors, which have achieved response times of less than a second and the capability to detect a broad spectrum of humidity levels, these sensors still face technical obstacles when applied to the realm of flexible wearable respiration detection. The primary challenges include the inherent limitations of rigid substrates and the complexity of lithography processes associated with MEMS sensors. Furthermore, the production of electrodes in most commercially accessible sensors relies on the use of precious metals and chemicals. Furthermore, most commercially available sensors are reliant on precious metals and chemicals for electrode fabrication. Finally, medical-grade respiratory monitoring devices currently lack portability. In light of the pressing demand for high-performance, cost-effective, and portable humidity sensors, laser-induced graphene (LIG) humidity sensors that utilize graphene oxide/LS thin films have emerged as a promising solution. These sensors offer several distinct advantages, including their flexibility, wide applicability, and the potential for cost-effective mass production. The integration of the sensing film with flexible LIG finger electrodes endows the sensor with the capacity to undergo folding and bending, rendering it optimal for incorporation into portable devices. The integration of the proposed sensor with a mouthpiece and an embedded microcontroller unit (MCU) facilitates the detection and counting of breaths. Furthermore, the ultra-high sensitivity of the sensor in high humidity environments ensures that the motion state sensing profiles measured can fulfil the requirements of high-frequency dynamic response.

Results and discussion

Synthetic procedures

Design of GO/LS-LIG humidity sensor. GO/LS-LIG humidity sensor electrode is mainly composed of LS–GO water molecule adsorption layer and LIG electrode layer (Fig. 1a), using a semiconductor laser engrave to modify the LS solution, in the process of laser etching, the laser causes a sharp increase in the local temperature, and many functional groups containing C–O and C═O bonds are broken, and the oxygen element is released in the form of gas (Fig. 1b). At the same time, the higher content of AL in the film undergoes C–C bond reorganisation by
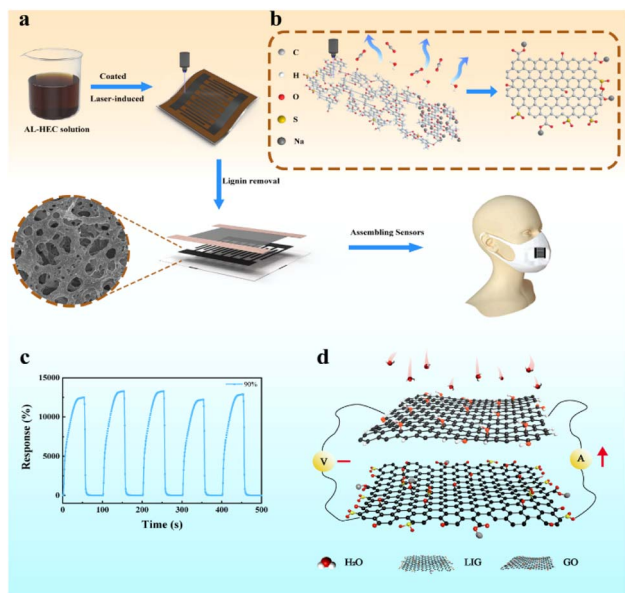
Paper

Fig. 1 (a) Schematic illustration of the fabrication process of the GO/LS-LIG humidity sensor. (b) Diagram of the molecular structure mechanism of LIG formation by laser etching of LS. (c) Recovery curve of GO−LS-3 response under 5 cycles at 90% humidity environments. (d) Schematic illustration of the humidity sensing mechanism.

reaction to form an aromatic backbone. The material is transformed from a sp^3 hybrid state to a more structurally ordered sp^2 hybrid state.

LS exhibits clear hygroscopic characteristics, enabling the adsorption of water molecules from the surrounding air. The combination of LS and GO results in the formation of additional hydrogen bond sites, which facilitates the adsorption of a greater number of water molecules onto the film. This, in turn, enhances the sensitivity and responsiveness of the material to fluctuations in humidity. Furthermore, the sensitivity can be augmented by depositing a GO–LS sensing solution onto a porous LIG electrode. The porous structure of the electrode increases the surface area of the GO that is susceptible to the effects of moisture. The deposition of the GO–LS sensing solution onto the highly porous structure forms rough films with a larger surface area than planar surfaces.

An illustration of the humidity-response mechanism is depicted in Fig. 1d. Under a consistent voltage, as humidity escalates, the electrode's resistance diminishes and the current intensifies, thereby altering the sensing signal across varying humidity conditions. With the escalation of humidity levels, water molecules are progressively adsorbed onto the surface of graphene oxide (GO) and lignosulfonate (LS). The LS molecules, abundant in highly hydrophilic sulfonic acid groups, effectively capture water molecules from the environment *via* hydrogen bonding and dipolar interactions. The sulfonic acid group facilitates the dissociation of hydrogen ions in the presence of water, forming an ion migration channel that markedly enhances the material's ionic conductivity. Additionally, the natural polymer framework of LS offers adsorption sites for water molecules, and its porous or cross-linked structure expedites the diffusion and

penetration of these molecules. The amalgamation of LS and GO yields a humidity sensor characterized by high responsiveness, minimal lag, repeatability, and stability (Fig. 1c). At reduced humidity levels, a limited number of water molecules adhere to the sulfonic acid groups of LS and the oxygen-functional groups of GO, partially dissociating to form localized ion migration pathways, which initiates a decrease in resistance. However, the absence of a continuous water layer on the sensor material's surface impedes the transfer of H_2O or H_3O^+ in the discontinuous regions, resulting in relatively minor impedance variations under low humidity conditions. As humidity continues to rise, a continuous water layer develops on the GO–LS interface, and the porous or cross-linked structure of LS promotes the transfer of H_2O or H_3O^+ ions. The natural macromolecular backbone of LS provides adsorption sites for water molecules, and the Grotthuss mechanism[28] describes the ion transport process involving proton transfer between H_2O and H_3O^+ within these water layers. The reaction is represented by the equation: $H_2O + H_3O^+ \rightarrow H_3O^+ + H_2O$. This ion-centric process results in a substantial reduction in impedance as relative humidity increases, and the swift ion transfer within the aqueous layer leads to a significant decrease in impedance, thereby enhancing the sensor's sensitivity. Nonetheless, due to the absence of a continuous electron conduction pathway in LS and the swelling effect of LS in high humidity conditions, which can influence the ion transport of water molecules and GO.

Characterisation of graphene electrodes

Pore structure analysis. Pore structure is one of the key factors affecting carbon electrodes, in order to evaluate the pore structure of LIG, N_2 adsorption desorption tests were carried out, and the specific surface area (SSA) and pore size distribution (PSD) of LIG, as shown in Fig. 2a, showed that LIG exhibits type IV adsorption isotherm and possesses a H3-type hysteresis loop. Meanwhile, the surface area increased with increasing laser power, and the maximum specific surface area (242.83 $m^2\ g^{-1}$) was obtained at a power of 100% (Fig. S1c†). At lower pressures ($P/P_0 < 0.01$), the adsorption capacity increased and the LIG surface presented a certain number of micropores. A good hysteresis loop was observed in the pressure range of 0.5–1. The Barrett–Joyner–Halenda (BJH) model was used to measure the pore size distribution of the material, and as shown in Fig. 2b, LIG-P100 possesses a large number of mesoporous structures and the main pore size is 3.99 nm, which is an obvious mesoporous material characteristic. Moreover, with the increase of laser power, the mesoporous pore size and total pore volume of LIG gradually increase (Fig. S1a–c†). The high specific surface area and rich mesoporous distribution of LIG provide a favorable structural foundation for electrode-sensing solution contact.

Conductivity analysis. In order to evaluate the conductivity of the LIG, a four-probe method was employed, with the laser scanning speed set between 50% and 70% and the laser intensity set between 50% and 100%. As illustrated in Fig. 2c, reducing scanning speed and increasing laser intensity result in a decline in the sheet resistance. The sheet resistance was found to be 10.37–12.99 $\Omega\ sq^{-1}$ under processing conditions with
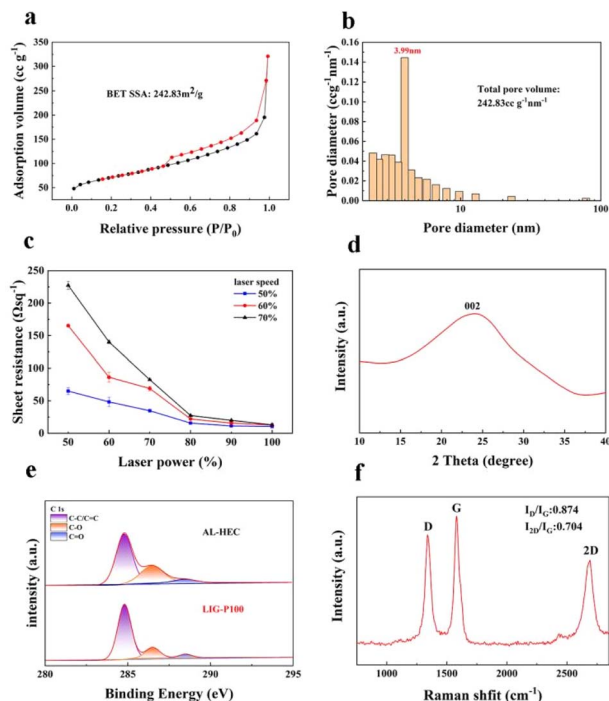
Fig. 2 (a) LIG-P100 adsorption desorption curve. (b) Pore size distribution of LIG-P100. (c) Resistance of LIG-P100 etched at different laser intensities using 50%, 60%, and 70% laser scanning speeds. (d) XRD pattern of LIG-P100. (e) C 1s XPS mapping of AL-HEC and LIG-P100. (f) Raman spectra of the LIG-P100.

Table 1 Quantitative ratios of C=O, C–OH and C–C fractions before and after laser processing of AL-HEC films

Chemical state	AL-HEC films (at %)	LIG-P100 (at %)
C–C	63.41%	78.55%
C–OH	31.07%	16.41%
C=O	5.53%	5.04%

atoms experienced dissociation during the laser etching process, resulting in alterations to the LIG functional groups.

Raman studies. As shown in Fig. 2f, the LIG is characterised by Raman spectroscopy, which contains three main signal peaks: peak G (1580 cm^{-1}) is an in-plane stretching oscillation induced by the sp^2 hybridisation of the C atoms, and peak D (1350 cm^{-1}) is induced by lattice defects in the LIG carbon atoms. The 2D peak (2670 cm^{-1}) is derived from the second-order band-boundary phonon and usually represents the layers of graphene. The degree of graphitization of carbon materials can be accurately assessed using the relative intensities (I_D/I_G) of the D and G peaks. The higher the I_D/I_G ratio, the more lattice impurities and defects are present in the graphene, with the lowest I_D/I_G ratio (0.874) being obtained when the applied laser power is increased to 100% (Fig. 2f and S3a–c†). The quality of graphene is assessed by the calculation of the I_{2D}/I_G intensity ratio in the Raman spectrum; the higher the I_{2D}/I_G ratio, the fewer the stacked layers of graphene, with the highest I_{2D}/I_G ratio (0.704) when the applied laser power is increased to 100%. The data indicate that the LIG samples exhibit regular sp^2 hybridisation and fewer stacked layers of graphite, and that the LIG prepared at a laser power of 100% best matches the characteristics of graphene. Due to the presence of the O element LIG still retains sp^3 hybridisation, which also corresponds to the findings of the XPS spectra.

Ttransmission electron microscopy analysis. The use of a low-magnification transmission electron microscope (TEM) allows for the clear observation of a graphite flake layer in the AL-HEC film (Fig. 3a), which exhibits a reduction in stacked layers

100% laser power. However, when the scanning speed was set to 50–60%, the resulting LIG exhibited some degree of cracking, which is not conducive to subsequent humidity sensor manufacturing.

X-ray diffraction. As Fig. 2d shows, the XRD peak at 25.4° in the centre of LIG-P50 is attributable to the (002) reflection, which represents the lattice reflection of graphene.

XPS analysis. As illustrated in Fig. 2e, the high-resolution C 1s XPS measurement spectra of the AL-HEC films primarily consist of signal peaks representing the C–C bond, the C=C bond near 284.8 eV, and the C–O and C=O bonds near 286.5 eV and 288.5 eV, respectively. Among these, the oxygen-containing functional groups in AL include C–O, C=O, and carboxyl groups, while HEC contains a substantial number of hydroxyl groups. Consequently, the C 1s spectra exhibit significant signal peaks corresponding to the C–C, C–O, and C=O bonds. Furthermore, it is evident that the intensity of the signal peaks for the C–C bonds of the AL-HEC films remains largely constant after the intensity of laser etching, while the intensities of the signal peaks for the C–O and C=O bonds are considerably reduced. The XPS analysis yielded analogous results in the case of varying power etching (Fig. S2a–d†). As illustrated in Table 1, a discernible shift in the quantitative ratios of C=O, C–OH, and C–C components was evident before and after laser treatment of the AL-HEC films. The atomic energy share of C–C exhibited a notable increase from 63.41% to 78.55%, accompanied by a reduction in the binding energies of C–OH and C=O to varying extents. It can be posited that the oxygen and carbon
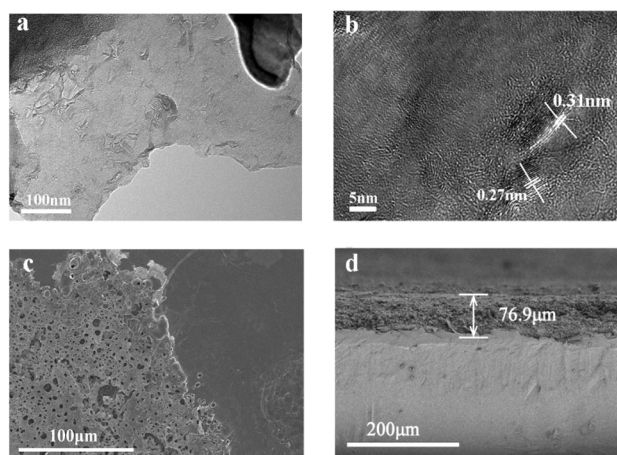

Fig. 3 (a) TEM images of LIG at different magnifications. (b) HRTEM image of the LIG. (c) SEM images of surface morphology at different magnifications of LIG. (d) SEM image of LIG cross section.

following laser etching. This observation corroborates the analytical conclusions drawn from Raman spectroscopy. As can be observed in the high-resolution transmission electron microscopy (HRTEM) image (Fig. 3b), the LIG displays an ordered lattice structure with a measured lattice spacing of 0.31 nm, which is in accordance with the findings of the XRD analysis.

Scanning electron microscopy analysis. SEM reveals the porous structure of the LIG surface, as illustrated in Fig. 3c. This is a three-dimensional porous structure formed by the irregular arrangement of the carbon skeleton, and the distribution of these pores is irregular. The irregular pore structure as well as the large specific surface area are beneficial to the adsorption of water molecules and the improvement of sensitivity. The cross-section of LIG is illustrated in Fig. 3d. It can be observed that carbonisation was carried out on a smooth PET film, and the thickness of the carbonised layer can be seen to be 76.9 μm by SEM image of the cross-section. There is no correlation between pore size and laser power; however, an increase in porous density is evident with elevated laser power, as illustrated in Fig. S1a–c.† These can indicate that the laser-treated surface forms a layered irregular porous structure, which contributes to the diffusion of water molecules.

Humidity sensing test

In order to evaluate the performance of the GO/LS-LIG humidity sensor, we conducted a series of experiments. Initially, as previously described, 10 mL of a 0.5 mg per mL GO solution was added to different masses of LS, with the LS added in a sequential manner. The sequence of additions was 0 mg, 1 mg, 5 mg, 10 mg, and 100 mg, and the resulting samples were labeled as GO–LS-n (n = 0, 1, 2, 3, and 4). In order to provide a quantitative description of the response of the aforementioned humidity sensor, we define response (R) and sensitivity (S) as follows:

$$R = R_{RH}/R_0 \tag{1}$$

$$S = (R_{RH} - R_0)/(RH_X - RH_0) \tag{2}$$

where, R_{RH} and R_0 are the sensor resistances at a given relative humidity and dry air, respectively is the humidity of the test environment, since the experimental control humidity is a dry environment, $RH_0 = 0$. The corresponding responsiveness as well as sensitivity can be calculated by using eqn (1) and (2).

Effect of the LS addition amount. The response of the assembled humidity sensor was evaluated at 80% relative humidity, and the results are presented in Fig. 4a. It is evident that as the quantity of LS incorporated increases, the response of the GO/LS-LIG humidity sensor rises from 17.70 (R_{RH}/R_0) to 42.74 (R_{RH}/R_0). The response time remains relatively constant. This phenomenon may be attributed to the fact that LS contains a considerable number of hygroscopic groups, and as the quantity of LS added increases, the capacity of the GO–LS composite sensing layer to capture free water molecules in the air gradually increases. It is noteworthy that when the amount added reaches 100 mg, the response level decreases to 6.04(R_{RH}/R_0) and the response time increases to 37.5 s. This phenomenon

can be attributed to the fact that the hydrophilic groups present in the LS structure can adsorb water molecules without significantly altering the material's conductivity. As the quantity of added substances increases, the possibility of trapping water molecules by oxygen functional group at the surface of graphene oxide is significantly reduced. This results in a reduction in the performance of the humidity sensor when an excess of LS is introduced. Comparisons with existing studies are listed (Table 2).

Analysis of hysteresis. Hysteresis can be defined as the discrepancy between the sensor output signals (*e.g.*, resistance, current or voltage) when the relative humidity undergoes an increase or decrease. The analysis of hysteresis in a humidity sensor represents a crucial stage in the evaluation of its performance. The response curve of the GO–LS-3 was measured in order to evaluate its hysteresis performance during a change in relative humidity from 11% to 90%. As illustrated in Fig. 4b, the documented response outcomes demonstrate that the sensor exhibits optimal performance in both the increase (adsorption) and decrease (desorption) of humidity within the range of 5% RH to 90% RH. The high degree of overlap between the two curves indicates that the sensor exhibits excellent hysteresis performance. The hysteresis can be calculated as follows: the maximum absolute value of the humidity hysteresis error is approximately 0.58% in the range of 11% RH to 97% RH, indicating that the sensor exhibits good reliability. This value is calculated using the following eqn (3):

$$H_{max} = F_{FS} - F_{FR} \tag{3}$$

where H_{max} is the difference between the outputs of forward and reverse operations, F_{FS} is the maximum output and F_{FR} is the minimum output.

Response and recovery characteristics of the sensor. The response and recovery behaviour of humidity sensors is contingent upon the adsorption and desorption processes of water molecules, making it a significant factor in evaluating sensor performance. The response time and recovery time refers to the time required for the sensors to reach 90% of the complete change in the adsorption and desorption states, respectively. The sensor was subjected to alternating cycles of dry conditions (0% RH) and humid conditions (90% RH), and the resulting change in sensor response was recorded. The response–recovery curve is illustrated in Fig. 4c. Upon exposure to 0% RH, the sensor exhibits a rapid initial rise in response, followed by a period of stabilisation as the RH rises to 97%. Following a period of stabilisation, the sensor is then exposed to a dry environment, resulting in a rapid decrease in response. The sensor exhibits a response time of 12 s and a recovery time of 2 s. As humidity levels rise, water molecules progressively adhere to the graphene oxide surface and the oxygen-containing functional groups within it. This process may entail a number of steps, including the diffusion of water molecules into the internal pore structure of the material and their subsequent formation of hydrogen bonds with surface functional groups. The aforementioned adsorption processes are relatively slow, particularly in environments with high humidity. Furthermore,
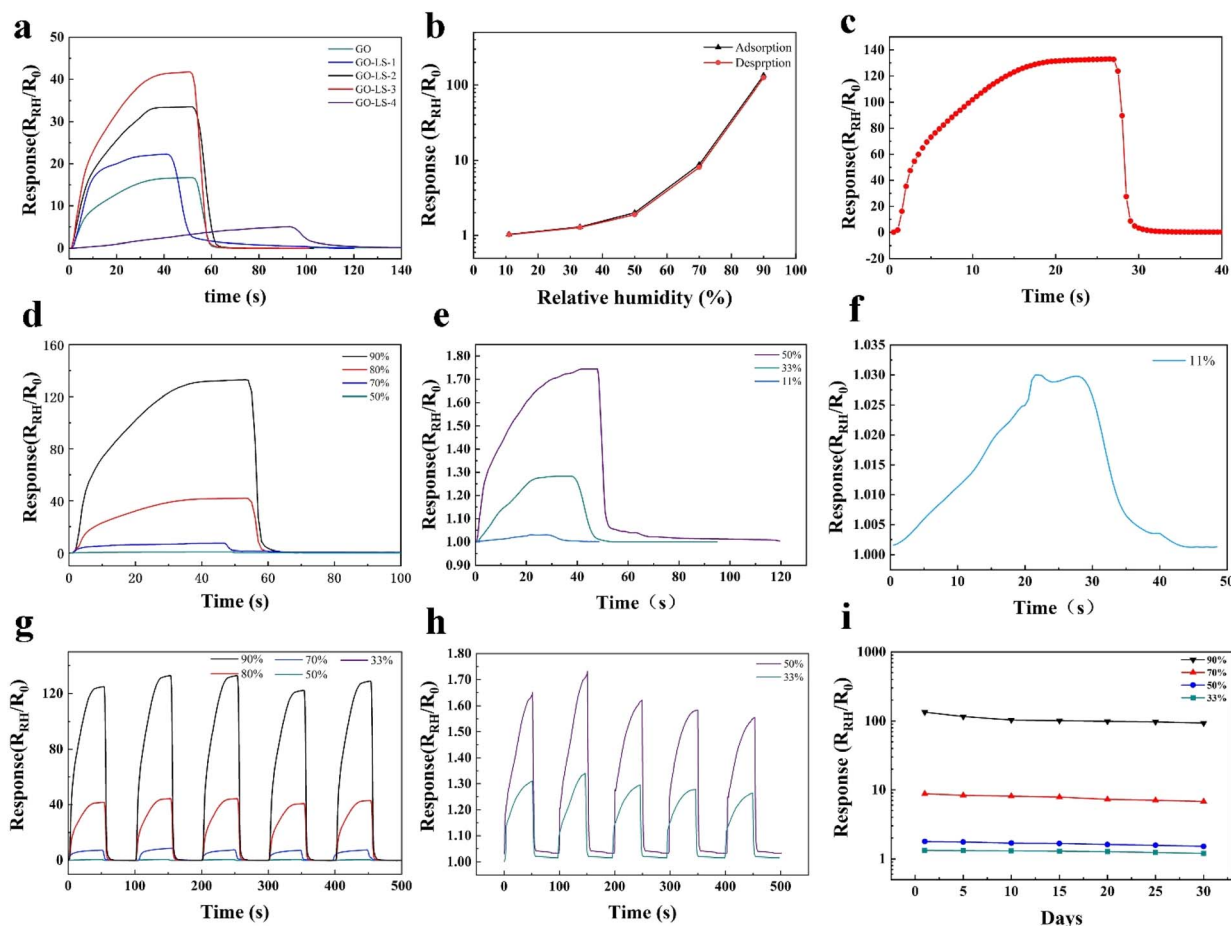
Fig. 4 (a) Humidity sensing curves for different LS additions. (b) Response and recovery curves for GO−LS-3. (c) Response curves corresponding to GO−LS-3 at different times. (d) Response recovery curve of GO−LS-3 at 50−90% RH. (e) Recovery curve of GO−LS-3 response at 11−50% RH. (f) Response recovery curve of GO−LS-3 at 11% RH. (g) Recovery curve of GO−LS-3 response under 5 cycles at different humidity environments and (h) amplification curve of recovery response curve under 5 cycles at 50% and 33% humidity environments. (i) Corresponding curves of GO−LS-3 in different humidity environments over a period of 30 days.

the adsorbed water molecules may accumulate in layers, resulting in an extended response time. In contrast, in dry environments, water molecules are prone to desorbing rapidly from the material surface. The interaction between water molecules and graphene oxide is primarily physical adsorption (hydrogen bonding), which results in a relatively weak interaction force. Consequently, in a dehumidified environment, water molecules can desorb from the surface more quickly, resulting in a shorter recovery time.

Sensor response analysis. The maximum response value is an important performance indicator of the sensor. As shown in Fig. 4d and e, in order to reach adsorption equilibrium, the humidity sensor should be placed in an environment corresponding to the relative humidity. Calculations show that the maximum responses to reach adsorption equilibrium are 1.029, 1.380, 1.831, 8.921, 42.517, and 139.192 for RH of 11%, 33%, 50%, 70%, 80%, and 90% RH, respectively. However, an interesting phenomenon has been observed, *i.e.*, no water film is formed on the surface of the sensors in the low-humidity region, mainly due to the fact that the water film is not formed on the surface of the sensors. Electronic conduction, the response level of the sensor starts to enhance dramatically as

Table 2 Comparison among different kinds of humidity sensors

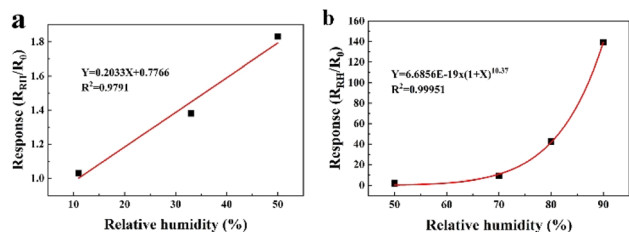| Material	Sensitivity	Humidity range	Response (s)/recovery (s)	LOD	Reference
Borophene–MoS$_2$	155 ($\Delta I/I_0$)	0–97%	2.5/3.1	LOD >0.9736% RH	41
rGO/MoS2	24.94 ($\Delta R/R_0$)	5–85%	6.3/30.8	LOD >0.0109% RH	42
GO-based	37.43%	11–97%	94/134	—	43
CNTs-paper	0.998/% RH	33–98%	0.5/90	—	44
LIG/poly	1700 kΩ/% RH	11–97%	4.2/6.8	—	45
LS/GO-LIG	147.73/% RH	11–90%	12/2	LOD >0.4429% RH	This work

Fig. 5 (a) Linear fitting equations at 11–50% relative humidity. (b) Fitted equations at 50–90% relative humidity.

the relative humidity increases, which also represents a sharp increase in ionic conductivity after the formation of a continuous water film and the hopping transport of protons (H^+) through the Grotthuss mechanism. Therefore, we calculated the obtained data separately, and in the low humidity region (11–50% RH), the sensor response shows a linear relationship ($Y = 0.2033X + 0.7766$, $R_2 = 0.9791$). In the high humidity region, the fitted equation for the sensor response is $Y = 6.6856E - 19x(1 + X)^{10.37}$, $R^2 = 0.99951$, and the fitted curve is shown in Fig. 5. The ultra-high response of the sensor response for the high humidity range facilitates our application in the direction of respiration detection (the relative humidity of human exhaled gas is close to 100% RH). According to our calculations, the

theoretical detection limit for the sensor is 0.4429% and the theoretical detection limit for quantification is 1.4764%. (See ESI data† for specific calculations[46–48]).

Sensor cyclic stability. The humidity sensor was subjected to repeated exposure to both dry and humid environments (33–90% RH) in order to test the reproducibility and reversibility of the sensor. The data presented in Fig. 4g and h was obtained from the continuous testing of five cycles, each with a 50-second cycle period. Upon returning to its original state, the relative humidity causes the sensor to return to a response value that is extremely close to the original value (the error is less than 0.1%). This demonstrates that the humidity sensing process is highly reversible. The response and recovery times remained largely unchanged across the five measurement cycles, indicating excellent reproducibility of the humidity response. Consequently, the GO–LS-LIG-based humidity sensor exhibits an ultra-fast response and fast recovery, as well as excellent repeatability and stability.

Long-term stability. The evaluation of sensors is contingent upon the assessment of stability, which is a pivotal criterion. The GO–LS-LIG humidity sensor was subjected to an environment with humidity levels of 33%, 50%, 70% and 90% for a period of 30 days. The maximum response was measured every five days, allowing the change in response over time to be determined. This
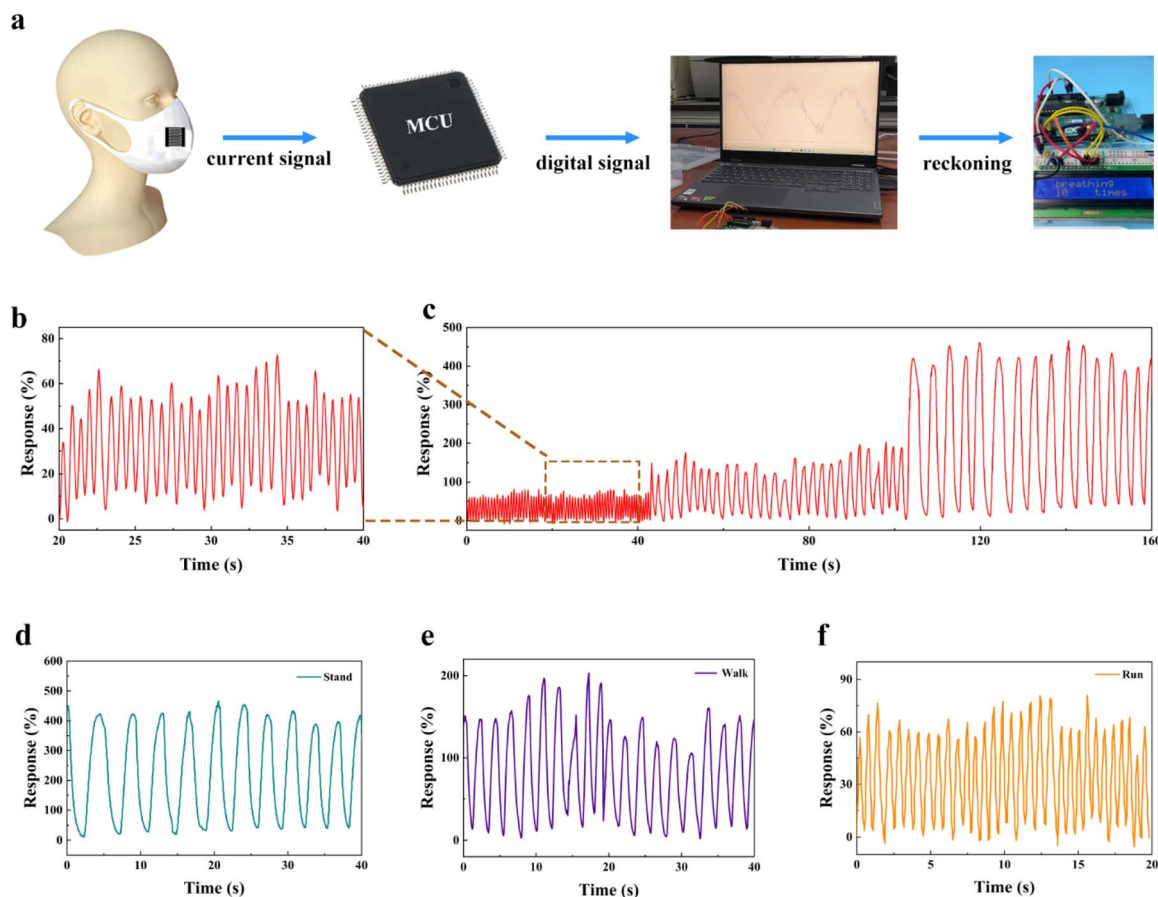

Fig. 6 (a) Schematic design of GO/LS-LIG mask breathing sensor. (b) Response curve of GO/LS-LIG human body in fast breathing condition. (c) Response curves of the human body in different respiratory states. (d–f) Respiration response curves during different motion states.

is illustrated in Fig. 4i. It can be observed that following a 30-day testing period, the change in response within each humidity range is minimal, thereby substantiating the assertion that the sensor exhibited excellent stability throughout this period.

Applications in respiratory monitoring

The humidity of human exhaled air is typically extremely high, approaching 100% relative humidity. This phenomenon is attributable to the absorption of moisture by the air as it traverses the lungs and respiratory tract, whereby the exhaled air attains a moisture content approaching saturation. The assembled GO/LS-LIG humidity sensor was placed into a disposable mask, as illustrated in Fig. 6a. The device was connected to an electrochemical workstation, and the response curves of the sensor to the human breathing were tested at a room temperature of 25 °C and an ambient humidity of 60% RH under fast, normal, and deep breathing states (Fig. 6b and c). During the fast breathing phase, the sensor's sensitivity to high humidity gases enabled it to record each breathing cycle with sufficient accuracy, even though it did not reach the maximum response value. The respiratory rate of the human body could then be calculated by determining the number of peaks per minute.

We proceeded to integrate the sensor into an embedded microcontroller unit (MCU). Upon the exhalation of gas by the human body, which causes a change in sensor resistance, the MCU (microcontroller unit) receives the analog signals and converts them into digital signals, thereby generating the appropriate commands to control the computer. In conjunction with the respiration cycle resulting from the alteration in resistance, the MCU-converted digital signal also undergoes a transformation. Through the implementation of a programmed "counting signal," each instance of the digital signal exceeding the "counting signal" results in the MCU's initiation of a data accumulation process, which is then displayed on the screen (for further details, please refer to Video 1†). We also tested the respiratory sensing under various exercise conditions, recording the sensing curves of the test subjects while standing, walking, and running (Fig. 6d–f). When standing, a relatively rounded curve is visible. During walking and running, the peaks and valleys of the sensing curve become sharper. In the case of running, due to the increased breathing rate, there are denser and sharper peaks and valleys, exhibiting a similar sensing curve trend to that observed during previous rapid breathing detection.

In the presence of high humidity gas, the resistance value of GO/LS-LIG undergoes significant changes, demonstrating high sensitivity. It can detect human respiration using only an MCU and provide valuable respiratory information under different motion conditions. This paves the way for advancements in portable respiratory monitoring devices.

Experimental

Materials

The alkaline lignin (L0082) was procured from TCI, while the sodium lignosulfonate was obtained from Macklin. The hydroxyethyl cellulose was sourced from Meryer, and the glycerol was purchased from Aladdin. The polyethylene terephthalate (PET) substrate was acquired from the Oudifu company.

Preparation of laser-induced graphene electrodes

A solution of 4.0 g of alkaline lignin (AL) in 50 mL of deionised water was prepared and mixed with 1.0 g of hydroxyethyl cellulose (HEC). Subsequently, 1.5 mL of glycerol should be added. The AL-HEC solution was then poured onto the PET plastic substrate and scraped into a film using a coating machine. The coating speed was set to 60 mm s^{-1} and the film thickness was set to 0.8 mm. Subsequently, the AL-HEC solution was subjected to a drying process at 60 °C for 30 min, after which the AL-HEC solution had undergone a process of film formation and had been affixed to the PET substrate. A semiconductor laser engraver (D3 laser engraver, DAJA) was selected for the laser etching of the AL-HEC film. The peak laser power of the laser engraver was 7 W, with the applied laser power representing a range of 50–100%. The scanning rate was set at 50–70% of the full scanning speed (100 mm s^{-1}). The LIG prepared at X% laser power is denoted as LIG-PX. The fork finger electrodes were designed to consist of 14 electrodes, with individual electrodes measuring 10.0 mm in length and 1.0 mm in width, and a spacing of 0.5 mm between electrodes. The fork finger electrodes were etched onto the surface of AL-HEC film to form LIG electrodes, and the remaining film was rinsed with deionised water to obtain the fork finger electrodes on the PET substrate, as illustrated in Fig. 1.

Humidity sensor preparation

GO was prepared by oxidising natural graphite powder (325 mesh, Qingdao Huatai Lubricant Seal Technology Co., Ltd, Qingdao, China) in accordance with the modified Hummers' method. A GO/LS mixture was prepared by adding varying masses of LS to a 10 mL solution of 0.5 mg per mL GO. Subsequently, 0.3 mL of the prepared solution was pipetted onto the surface of the forked electrode and dried at 60 °C. The solution was then subjected to a drying process at 60 °C. Following this, copper foil was attached to both sides of the forked electrode, thus completing the assembly of the sensor.

Characterisation of materials

The square resistance of the LIGs was determined utilising a four-point probe resistivity measurement system (RTS-2, Guangzhou Four Points Technology Co., Ltd, Guangzhou, China). Scanning electron microscope images were obtained using a field emission scanning electron microscope (Regulus 8100, Hitachi, Japan), and transmission electron microscopy observations were conducted using a Hitachi H-7650 B transmission electron microscope operated at 80 kV. Furthermore, high-resolution transmission electron microscopy (HRTEM) imaging was conducted using a FEI Tecnai F20 HRTEM at 200 kV. Raman spectra were obtained using a confocal Raman microscope (Horiba Jobin Yvon, France) with a 532 nm laser and a 50× objective lens, with wave numbers ranging from 500 to 2800 cm^{-1}. X-ray diffraction

was conducted using a Rigaku Ultima IV diffractometer (Japan), while XPS measurements were performed with a K-Alpha spectrometer (Thermo Fisher Scientific, USA) with a beam size of 400 μm. The specific surface area was calculated using the BET method with a BUILDER Kubo-X1000 tester, based on nitrogen adsorption–desorption analysis.

Humidity sensing measurements

Ambient humidity conditions ranging from 40% to 90% were provided by a constant temperature and humidity chamber (HWS-80, Zhejiang Shangcheng, China). When a relative humidity of less than 40% was desired, we added 50 mL of saturated lithium chloride to one of the sealed solvents and fifty mL of saturated magnesium chloride solution to the other, which was used to create a relative humidity of 11% *versus* 33%. A 0% RH environment was obtained by using phosphorus pentoxide (P_2O_5) powder as a desiccant. The RH response of the sensor was achieved by humidifying the sensor in a constant temperature and humidity chamber and then quickly transferring it to a sealed container at 0% RH to remove water molecules. This iterative process of moisture absorption and release is defined as the humidification–dehumidification cycle. The resistance change of the prepared humidity sensor was measured using an electrochemical workstation (CHI 660E, ChenHua).

Conclusions

By integrating mass-producible LEG, graphene oxide and lignin-based materials, we have developed a flexible humidity sensor. With an enhanced surface area of 242.83 m² g⁻¹ and a rich mesoporous structure, LIG provided the structural basis for sensor performance. The hygroscopicity of LS significantly improves the response time of the sensors, enabling a rapid response time of 12 seconds and a recovery time of 2 seconds at 90% relative humidity. Notably, the sensors exhibit precise and linear response signals across various humidity levels, demonstrating their reliability in sensing applications. Furthermore, the sensor demonstrates good repeatability and stability during testing. It can also be embedded into microcontrollers to develop portable humidity response devices, which have good application prospects in the field of smart materials and provide new ideas for the development of sensors for lignin-based materials.

Data availability

All data generated or analyzed in this study are included in this manuscript document as well as in the ESI.†

Conflicts of interest

There are no conflicts to declare.

Acknowledgements

Notes and references

1 M. Tekcin, D. R. T. Hamzaoglu and S. Kursun, *Flexible Printed Electron.*, 2023, **8**, 035003.
2 J.-W. Han, B. Kim, J. Li and M. Meyyappan, *J. Phys. Chem. C*, 2012, **116**, 22094–22097.
3 M. Y. Cho, S. Kim, I. S. Kim, E. S. Kim, Z. J. Wang, N. Y. Kim, S. W. Kim and J. M. Oh, *Adv. Funct. Mater.*, 2020, **30**, 1907449.
4 Y. Zhao, X.-G. Li, X. Zhou and Y.-N. Zhang, *Sens. Actuators, B*, 2016, **231**, 324–340.
5 S. R. Vaughan, N. C. Speller, P. Chhotaray, K. S. McCarter, N. Siraj, R. L. Pérez, Y. Li and I. M. Warner, *Talanta*, 2018, **188**, 423–428.
6 D. Pawar and S. N. Kale, *Microchim. Acta*, 2019, **186**, 1–34.
7 Q. Zheng, J.-h. Lee, X. Shen, X. Chen and J.-K. Kim, *Mater. Today*, 2020, **36**, 158–179.
8 P. Zhou, L. Chen, L. Yao, M. Weng and W. Zhang, *Nanoscale*, 2018, **10**, 8422–8427.
9 P. Zhu, Y. Liu, Z. Fang, Y. Kuang, Y. Zhang, C. Peng and G. Chen, *Langmuir*, 2019, **35**, 4834–4842.
10 L. Lu, B. Yang and J. Liu, *Chem. Eng. J.*, 2020, **400**, 125928.
11 K. Sahoo, B. Mohanty, A. Biswas and J. Nayak, *Mater. Sci. Semicond. Process.*, 2020, **105**, 104699.
12 C. Huo, H. Chen, L. Chen, S. Yang, P. Cui and J. Song, *J. Electron. Mater.*, 2024, **53**, 5238–5245.
13 C. Yu, Y. Wu, X. Liu, F. Fu, Y. Gong, Y.-J. Rao and Y. Chen, *Sens. Actuators, B*, 2017, **244**, 107–113.
14 S. Hu, S. Wu, C. Li, R. Chen, E. Forsberg and S. He, *Sens. Actuators, B*, 2020, **305**, 127517.
15 A. J. Ragauskas, G. T. Beckham, M. J. Biddy, R. Chandra, F. Chen, M. F. Davis, B. H. Davison, R. A. Dixon, P. Gilna and M. Keller, *Science*, 2014, **344**, 1246843.
16 A. Duval and M. Lawoko, *React. Funct. Polym.*, 2014, **85**, 78–96.
17 L. Cao, K. Iris, Y. Liu, X. Ruan, D. C. Tsang, A. J. Hunt, Y. S. Ok, H. Song and S. Zhang, *Bioresour. Technol.*, 2018, **269**, 465–475.
18 S. Laurichesse and L. Avérous, *Prog. Polym. Sci.*, 2014, **39**, 1266–1290.
19 M. Witzler, A. Alzagameem, M. Bergs, B. El Khaldi-Hansen, S. E. Klein, D. Hielscher, B. Kamm, J. Kreyenschmidt, E. Tobiasch and M. Schulze, *Molecules*, 2018, **23**, 1885.
20 J. Becker and C. Wittmann, *Biotechnol. Adv.*, 2019, **37**, 107360.
21 J. H. Lora and W. G. Glasser, *J. Polym. Environ.*, 2002, **10**, 39–48.
22 E. Ten and W. Vermerris, *J. Appl. Polym. Sci.*, 2015, **132**, 42069.
23 M. F. El-Kady, V. Strong, S. Dubin and R. B. Kaner, *Science*, 2012, **335**, 1326–1330.
24 A. Lamberti, F. Perrucci, M. Caprioli, M. Serrapede, M. Fontana, S. Bianco, S. Ferrero and E. Tresso, *Nanotechnology*, 2017, **28**, 174002.
25 H. Tai, Z. Duan, Y. Wang, S. Wang and Y. Jiang, *ACS Appl. Mater. Interfaces*, 2020, **12**, 31037–31053.

26 P. Zhu, Y. Kuang, Y. Wei, F. Li, H. Ou, F. Jiang and G. Chen, *Chem. Eng. J.*, 2021, **404**, 127105.

27 T. Aro and P. Fatehi, *ChemSusChem*, 2017, **10**, 1861–1877.

28 S. Hajian, X. Zhang, P. Khakbaz, S.-M. Tabatabaei, D. Maddipatla, B. B. Narakathu, R. G. Blair and M. Z. Atashbar, *IEEE Sens. J.*, 2020, **20**, 7517–7524.

29 L. Duan, D. R. D'hooge and L. Cardon, *Prog. Mater. Sci.*, 2020, **114**, 100617.

30 J. Meng and Z. Li, *Adv. Mater.*, 2020, **32**, 2000130.

31 K. S. Novoselov, A. K. Geim, S. V. Morozov, D.-E. Jiang, Y. Zhang, S. V. Dubonos, I. V. Grigorieva and A. A. Firsov, *Science*, 2004, **306**, 666–669.

32 A. K. Geim and K. S. Novoselov, *Nat. Mater.*, 2007, **6**, 183–191.

33 F. Schedin, A. K. Geim, S. V. Morozov, E. W. Hill, P. Blake, M. I. Katsnelson and K. S. Novoselov, *Nat. Mater.*, 2007, **6**, 652–655.

34 A. K. Geim, *Science*, 2009, **324**, 1530–1534.

35 K. P. Loh, Q. Bao, G. Eda and M. Chhowalla, *Nat. Chem.*, 2010, **2**, 1015–1024.

36 Y. Tu, L. Zhao, J. Sun, Y. Wu, X. Zhou, L. Chen, X. Lei, H. Fang and G. Shi, *Chin. Phys. Lett.*, 2020, **37**, 066803.

37 G. Zhu, Z. Huang, L. Zhao and Y. Tu, *Nanoscale*, 2021, **13**, 15231–15237.

38 R. Alrammouz, J. Podlecki, A. Vena, R. Garcia, P. Abboud, R. Habchi and B. Sorli, *Sens. Actuators, B*, 2019, **298**, 126892.

39 S. Yan, D. Shen, M. A. A. Newton, S. Zhu and B. Xin, *Colloids Surf., A*, 2024, **695**, 134198.

40 D. J. Late, Y.-K. Huang, B. Liu, J. Acharya, S. N. Shirodkar, J. Luo, A. Yan, D. Charles, U. V. Waghmare and V. P. Dravid, *ACS Nano*, 2013, **7**, 4879–4891.

41 C. Hou, G. Tai, Y. Liu, Z. Wu, Z. Wu and X. Liang, *J. Mater. Chem. A*, 2021, **9**, 13100–13108.

42 S. Y. Park, Y. H. Kim, S. Y. Lee, W. Sohn, J. E. Lee, D. H. Kim, Y.-S. Shim, K. C. Kwon, K. S. Choi and H. J. Yoo, *J. Mater. Chem. A*, 2018, **6**, 5016–5024.

43 D. Zhang, J. Tong and B. Xia, *Sens. Actuators, B*, 2014, **197**, 66–72.

44 A. Liang and X. Chen, *J. Mater. Chem. A*, 2024, **12**, 29081–29091.

45 J. Wang, N. Wang, D. Xu, L. Tang and B. Sheng, *Sens. Actuators, B*, 2023, **375**, 132846.

46 J. Li, Y. Lu, Q. Ye, M. Cinke, J. Han and M. Meyyappan, *Nano Lett.*, 2003, **3**, 929–933.

47 V. Dua, S. P. Surwade, S. Ammu, S. R. Agnihotra, S. Jain, K. E. Roberts, S. Park, R. S. Ruoff and S. K. Manohar, *Angew. Chem.*, 2010, **122**, 2200–2203.

48 Y. H. Kim, S. J. Kim, Y.-J. Kim, Y.-S. Shim, S. Y. Kim, B. H. Hong and H. W. Jang, *ACS Nano*, 2015, **9**, 10453–10460.